

BACKGROUND IMAGE—iGRAPHIC STOCK

# An All-Metal, 3-D-Printed CubeSat Feed Horn

*An assessment of performance conducted at 118.7503 GHz using a robotic antenna range.*

Joshua A. Gordon, David R. Novotny, Michael H. Francis, Ronald C. Wittmann, Miranda L. Butler, Alexandra E. Curtin, Jeffery R. Guerrieri, Lavanya Periasamy, and Albin J. Gasiewski

Digital Object Identifier 10.1109/MAP.2017.2655574  
Date of publication: 21 February 2017

Three-dimensional (3-D) printing is finding applications across many areas and may be a useful technology for antenna fabrication for cube satellites (CubeSats). However, the quality of an antenna produced using 3-D printing must be considered if this technology can be relied upon. We present gain and far-field pattern results for the feed horn of the radiometer payload of the CubeSat PolarCube. The corrugated feed horn is constructed from AlSi10Mg alloy and fabricated using powder bead fusion (PBF). Measurements were performed at the atmospheric oxygen line of 118.7503 GHz with the National Institute of Standards and Technology (NIST) Configurable Robotic Millimeter-Wave Antenna (CROMMA)

facility in Boulder, Colorado. A comparison of these measurements to theoretical predictions provides an assessment of the performance of the feed horn.

## CubeSat OVERVIEW

CubeSats offer an accessible and effective platform for a wide variety of space-based applications. Many off-the-shelf components are allowing fast prototyping of CubeSats and subsystems. Space-based applications benefit from millimeter waves (mm-waves) because shorter wavelengths allow for low diffraction, high bandwidth, and small form factor. Radiometers rely on mm-waves due to the ubiquity of passive blackbody emissions and the existence of atmospheric spectral features. Emerging applications, such as global Internet [1], are projected to use constellations of more than 1,000 CubeSats operating above 100 GHz for satellite-to-satellite and satellite-to-ground communications. Instrumentation and scientific needs often drive antenna designs that are not available off the shelf, as opposed to many other CubeSat components. Therefore, antennas must be designed on a case-by-case basis to achieve desired performance characteristics, such as gain and sidelobe level.

The ability to quickly prototype, fabricate, and test mm-wave antennas with the same ease as obtaining other off-the-shelf components would allow CubeSats to be used more readily. Recent advances in 3-D printing could enable antennas to be quickly custom fabricated with complex structure to meet specific application needs. However, the quality and performance of printed antennas is not as well established as more traditional fabrication techniques, such as machining and electroforming. Fabrication tolerances become more precise at high mm-wave frequencies. Edge fidelity of apertures, corrugated features, and so forth, can be challenging to reproduce because 3-D printing creates inherently rough surfaces. This could impact antenna performance. Depending on the performance requirements, tradeoffs in antenna performance may be offset by the conveniences of 3-D printing. In this article, we present a comparison between the measured and theoretical gain and far-field pattern at 118.7503 GHz of an all-metal 3-D-printed conical corrugated feed horn antenna that will be used in the radiometer payload of the PolarCube CubeSat.

## PolarCube SATELLITE

PolarCube is a three-unit CubeSat satellite with a payload composed of an eight-channel, double-sideband 118.75-GHz scanning passive microwave temperature sounder, MiniRad [2], [3]. Radiometric observations near the 118.7503-GHz oxygen line are used to profile atmospheric temperature [4], [5]. The radiometer payload is made up of a spinning offset paraboloidal main reflector and a stationary conical corrugated feed horn. The main reflector is an off-axis ellipse with a projected circular aperture of 8 cm. The feed horn + reflector combination is intended to have a gain of 38.03 dB. Figure 1 shows a cross-sectional view of the PolarCube optical front end with corrugated feed horn and deployable parabolic reflector shown in yellow. The feed horn couples radiation from the main reflector to the radiometer receiver electronics. The spinning reflector configuration allows for maximum aperture area resulting in a



**FIGURE 1.** A cross-sectional view of the optical train front end of the PolarCube CubeSat radiometer. The parabolic reflector and 3-D-printed metal feed horn are highlighted in yellow.

3-dB footprint size of 16 km for nadir observation. The reflector is supported by a single strut that minimizes sidelobe scattering and antenna temperature uncertainty.

## FEED HORN

### 3-D PRINTING

In recent years, 3-D printing in plastic has led to the investigation of dielectric microwave structures, such as reflectarrays [6] and bandgap materials [7]. Metal-coated 3-D-printed plastic antennas [8] have also been demonstrated for use in mm-wave and terahertz applications. The structural integrity offered by solid metal construction is advantageous, however, and 3-D printing of pure metal alloys is also being investigated for constructing antennas. 3-D printing using metal alloys has many of the same advantages as polymer printing, with added structural integrity and possibly better longevity. It is not clear whether the fidelity obtainable with current metal printing technology is adequate for fabricating mm-wave antennas and what tradeoffs may need to be considered.

The PolarCube feed horn, shown in Figure 2, was made from the aluminum alloy AlSi10Mg and fabricated using PBF (colloquially referred to as *metal 3-D printing*). AlSi10Mg is optimized for the PBF process and was chosen for its strength, hardness, and because its structural integrity is maintained even when formed into thin and complex shapes. Furthermore, this alloy can be machined and polished after the PBF process without loss of structural integrity. No supports were needed during the fabrication of the feed horn, as the build direction was set such that the horn cone axis was aligned with gravity. After PBF, the horn was finished with a glass bead blast to reduce surface roughness from an Ra of 300  $\mu\text{in}$  to 125  $\mu\text{in}$ . The waveguide flange screw holes were made using a standard tap.

## ANTENNA DESIGN

The horn was designed per [9] to support an  $HE_{11}$  hybrid mode that is well matched to the main reflector. The horn is fed by



a rectangular WR-08 waveguide that transitions to a circular cross section into the conical flare. This transition is further complicated in that it includes the necessary tilt angle of  $17^\circ$  used to angle the feed horn toward the main reflector. The

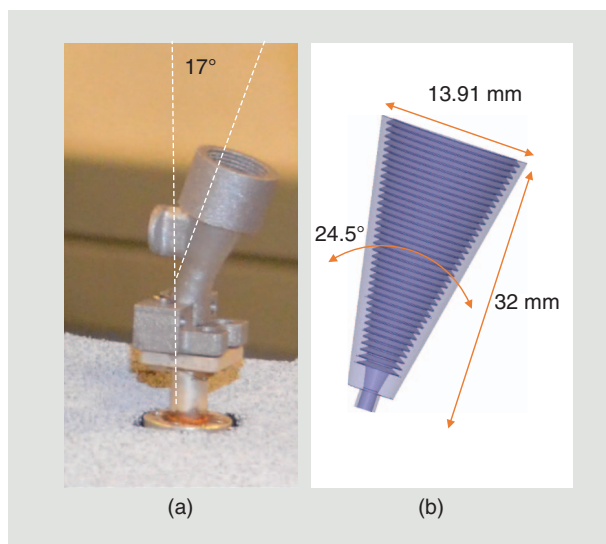


**FIGURE 2.** (a) The 3-D-printed metal AlSi10Mg feed horn. (b) A schematic showing the dimension of the feed horn conical section. (Photo courtesy of Josh Gordon, NIST.)

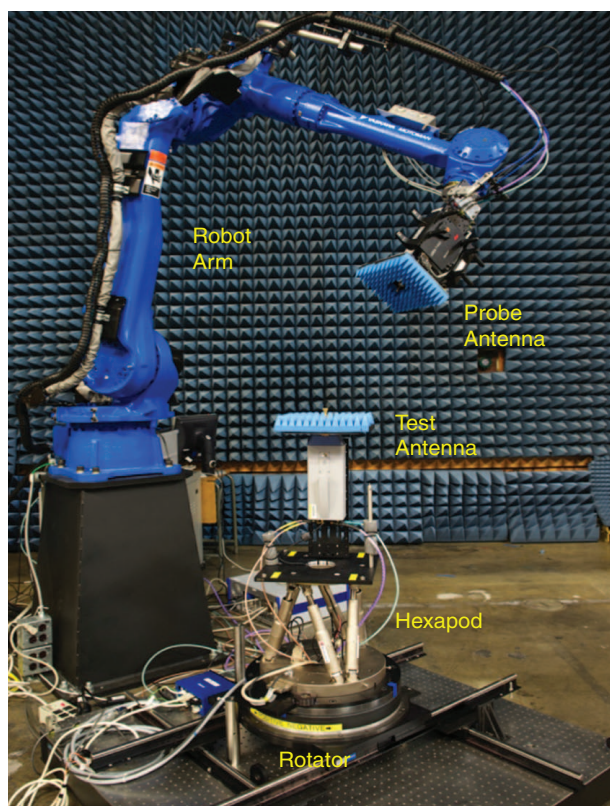


**FIGURE 3.** The CROMMA facility. The main system components are shown: robotic arm, hexapod, rotator table, probe, and test antenna locations. (Photo courtesy of Curt Suplee, NIST.)

feed horn was designed with a circular diameter aperture of  $D = 13.91$  mm, cone angle  $\theta_h = 24.5^\circ$ , and length (aperture-to-cone apex)  $L = 32$  mm. The corrugations were optimized to a depth of  $\approx 0.28\lambda$  with a spacing of  $\approx \lambda/3$  and given a chamfer angle of  $\approx 30^\circ$  to provide proper mode conversion from the circular waveguide into the cone section. The horn, therefore, has many submillimeter and intricate mechanical features that make 3-D printing worth investigating as a fabrication option.

## MEASUREMENT SETUP

### ROBOTIC ANTENNA RANGE

Measurements were performed using the CROMMA [10]–[13] at NIST. The use of robotics allows multiple-scan geometries to be executed autonomously using a single antenna alignment and electrical calibration. This capability allows for rapid antenna characterization because both near-field and in situ extrapolation measurements could be made without the need to change setups, realign antennas, or recalibrate. With CROMMA, near-field measurements are achieved by using the robotic arm (see Figure 3) to scan a  $\mu = \pm 1$  probe antenna [14] over a surface about the antenna under test (AUT). The AUT sits atop a six-axis hexapod and rotator. To perform spherical scanning, the robot arm is moved along an arc ( $\theta$  direction) while the AUT can be rotated ( $\phi$  direction), creating a spherical geometry. Extrapolation scans are performed by scanning the probe along a linear path bore-sight between the AUT and probe antennas. A laser tracker and 6 degrees of freedom (6DoF) optical targets are used to provide spatial metrology of the coordinate frames of the probe antenna, AUT, robot, hexapod, and rotator. Spatial metrology software was used to capture and manipulate laser tracker data for the alignment of the probe and AUT during measurements. The robotic arm can reconfigure itself based on this spatial metrology feedback with an accuracy of  $<25 \mu\text{m}$ , which enables autonomous changes between near-field and extrapolation scan geometries [10], [15]. This was used to perform in situ extrapolation measurements in series with the near-field measurement. This sped up antenna characterization and allowed the extrapolation data to be used as diagnostics to optimize the near-field measurement (discussed in the “Extrapolation Measurements” section).

The  $\mu = \pm 1$  probe antenna and feed horn apertures were directly measured with a laser tracker and Pixel Probe [16] (a machine-vision-based touchless laser tracker probe). Images of the feed horn from the Pixel Probe during the alignment process are shown in Figure 4. The corrugations and surface roughness resulting from the 3-D printing process are clearly visible. In Figure 4(c), the white arrow points to a measurement location on the aperture where the active pixel (highlighted blue) of the Pixel Probe was placed. The size of the blue pixel corresponds to the effective spatial resolution (i.e., pixel footprint). For this alignment, the Pixel Probe resolution used was  $\approx 30 \mu\text{m}$  ( $\lambda/85$  at 118 GHz). A series of measurements around the aperture perimeter were taken to construct the aperture geometry (see Figure 5) and pose of the feed horn after the initial setup. Fitting a circle to these measurements produced an aperture radius of 13.98 mm. This is consistent with the intended

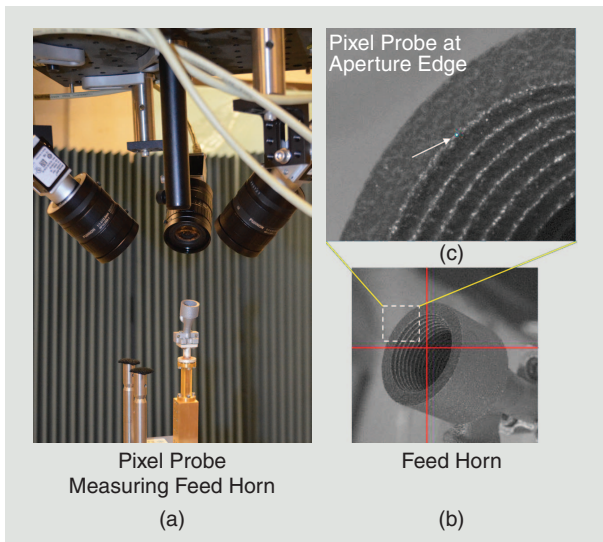


**FIGURE 4.** (a) The alignment measurement of the feed horn using the Pixel Probe. (b) The feed horn as seen through one of the cameras of the Pixel Probe, where it is first centered in the red crosshairs. (c) The Pixel Probe is positioned to measure the aperture edge. The white arrow points to the active pixel, highlighted in blue, that is used to measure a location on the edge of the aperture. Also visible is the surface roughness due to the 3-D printing process. (Photos courtesy of Josh Gordon, NIST.)

aperture diameter of  $D = 13.91$  mm and the known roughness of the aperture edge due to the 3-D printing process. Translation and orientation offset errors in the initial setup alignment of the feed horn from the ideal measurement alignment were calculated using the spatial metrology software. These offsets were then input to the hexapod to align the center of the feed horn aperture to the origin of the spherical scan geometry while keeping the  $17^\circ$  tilt angle in  $\theta$ . Spatial measurements of the feed horn aperture and resulting coordinate system are shown in Figure 5. The scan arc and linear path for the spherical near-field and extrapolation measurements, respectively, are shown in Figure 6. Following these two paths are the stacks of coordinate frames that result from measuring the 6-DoF laser tracker target when tracking the probe antenna.

## MM-WAVES

A four-port 50-GHz vector network analyzer (VNA) and WR-08 frequency extenders were used to generate and detect mm-waves during measurements. The VNA was set up for two-port measurements. A short, offset-short, load unknown through electrical calibration was performed over the full WR-08 band (90–140 GHz). The  $\pm 180^\circ$  phase ambiguity from the unknown through was able to be removed because of the full bandwidth calibration. The radio-frequency cables on the probe and AUT sides were stabilized with appropriate service loops and mounting fixtures. The VNA was triggered externally by the robot controller input/output trigger output and preconditioned with a pulse generator to adjust timing of the VNA with the robot position. Amplitude and phase of S-parameters were captured at each probe measurement location along the spherical near-field scan arc.

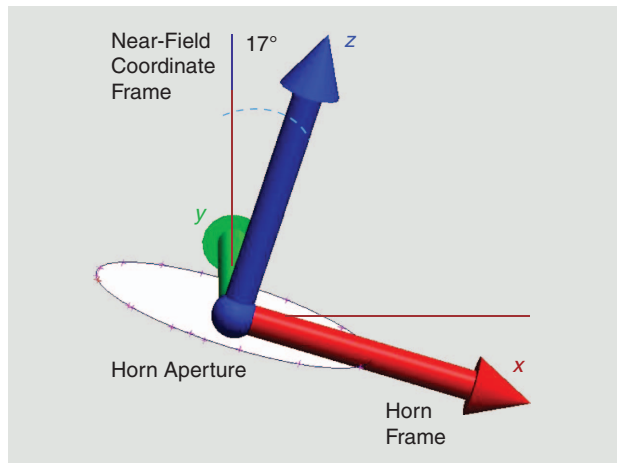


**FIGURE 5.** The feed horn aperture and corresponding coordinate system are shown relative to the near-field measurement coordinate system. The red x's on the feed horn aperture mark Pixel Probe measurements that were used to determine the location and orientation of the feed horn. Actual horn aperture diameter was measured to be 13.98 mm.

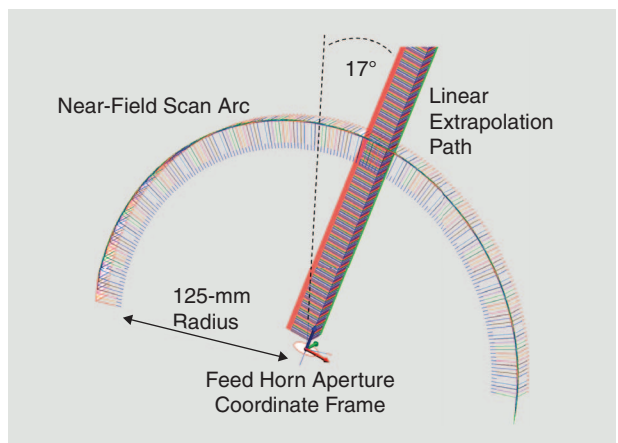


**FIGURE 6.** The spatial metrology from the laser tracker showing the feed horn aperture and the dual scan geometries executed by the robotic arm. The stacks of coordinate frames for each probe antenna location along the extrapolation path and near-field arc are shown. The extrapolation path follows the  $17^\circ$  tilt angle of the feed horn aperture.

## ANTENNA MEASUREMENTS

### EXTRAPOLATION MEASUREMENTS

Extrapolation measurements [17] were performed to determine the gain of the feed horn as well as to optimize the near-field scan radius for maximum dynamic range. During a near-field measurement, dynamic range can be increased by reducing the probe-to-AUT distance. However, this comes at the cost of increased mutual coupling and reflections between the probe and AUT, which reduces signal quality. The  $HE_{11}$  mode of this feed horn has inherently very low sidelobes, so it was important to increase the dynamic range (as measured from the main beam to noise floor) such that any sidelobe structure could be detected beyond  $\pm 30^\circ$  of the main beam.

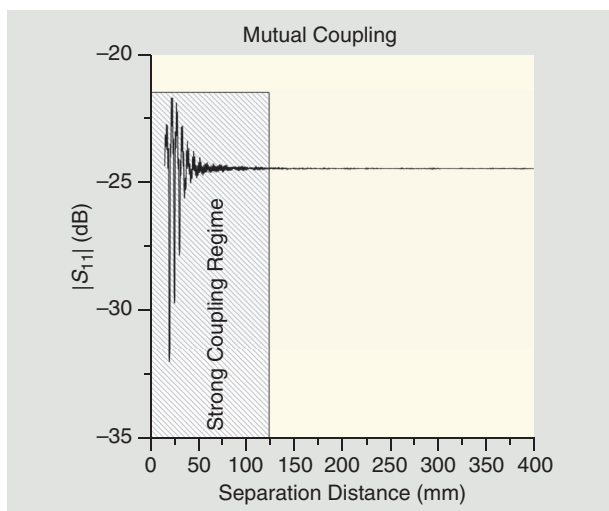


**FIGURE 7.** The  $|S_{11}|$  in decibels plotted over the horn-to-probe separation distance. Oscillations show reflections caused by the mutual coupling between the probe and feed horn. The edge of the strong coupling regime (shading) at a distance of 125 mm is where the mutual coupling is reduced to  $\Delta |S_{11}| \leq 0.1$  dB (peak to peak).

Mutual coupling strength was determined from observing the oscillations in  $|S_{11}|$  in the extrapolation measurement. This is shown in Figure 7.

Data were taken every  $400 \mu\text{m}$  ( $\approx \lambda/6$  at 118.7503 GHz) as the probe was translated over a distance ranging from 15 to 400 mm to the feed horn aperture. The separation distance at which these oscillations dropped to  $\Delta |S_{11}| \leq 0.1$  dB (peak to peak) was taken as the closest radius usable for the near-field

**TABLE 1. MEASUREMENT PARAMETERS.**

Scan Type	Spherical Scan
$\theta$ range	$\pm 90^\circ$
$\phi$ range	$\pm 360^\circ$
$\Delta\theta$	$1^\circ$
$\Delta\phi$	$1^\circ$
Operating frequency	118.7503 GHz
Wavelength	2.54 mm
Measurement radius	125 mm
Positional accuracy (root mean square)	$\lambda/100 (< 25 \mu\text{m})$
Dynamic range (from main beam peak to noise floor)	70 dB

measurement. This turned out to be at a distance of 125 mm. The gain of the feed horn as determined from the extrapolation measurement was  $G_{\text{extrap}} = 20.32 \text{ dB} \pm 0.5 \text{ dB}$ .

### SPHERICAL NEAR-FIELD MEASUREMENTS

The far-field pattern of the feed horn was also measured (see Table 1). Beam spillover and sources of leakage into the optical train can affect radiometer calibration, so it was important to characterize as much of the off-axis beam as possible. For Polar-Cube, the angle subtended by the main reflector as seen by the feed horn is  $\approx 35^\circ$ . Knowledge of the energy spillover outside this region is taken into account during radiometer calibration. Therefore, spherical near-field measurements were performed

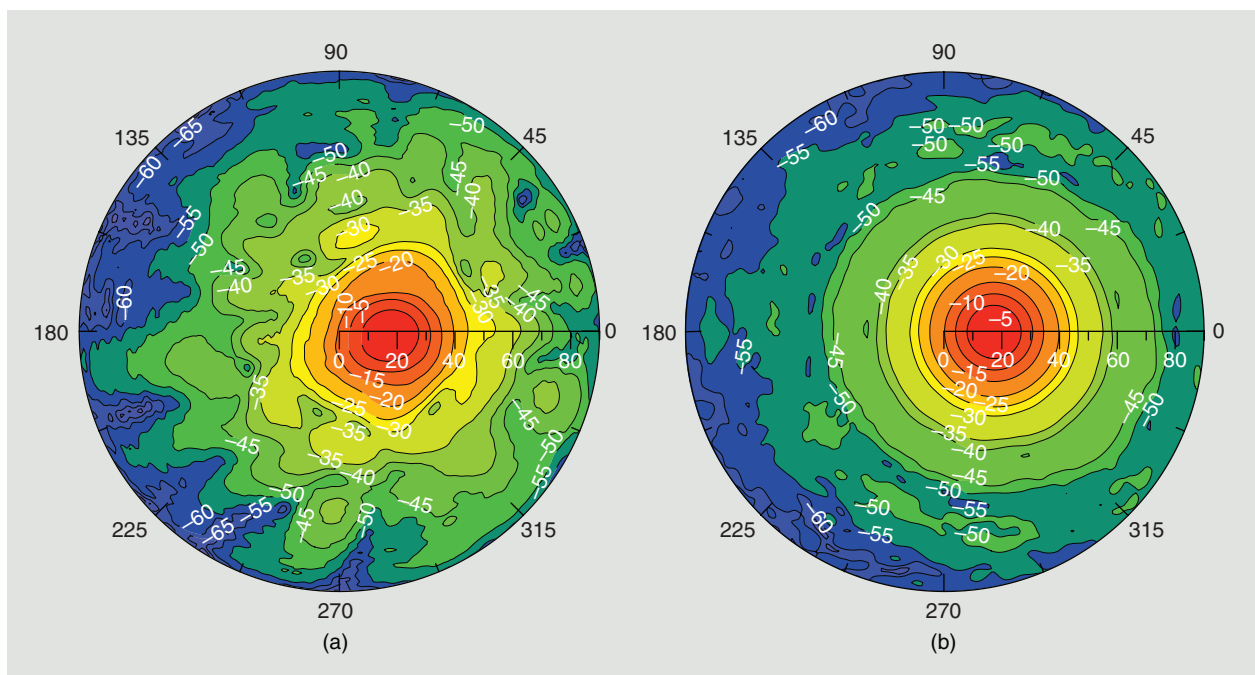


**FIGURE 8.** The far-field patterns of the magnitude of the total electric field over the front hemisphere of the feed horn. Patterns are normalized to the peak value. (a) The measured pattern. (b) The simulated pattern.



as opposed to planar [18] measurements to provide large solid-angle coverage. With CROMMA, the front hemisphere ( $0 \leq \theta \leq +90^\circ$ ,  $0 \leq \phi \leq 360^\circ$ ) was able to be covered, which allowed off-axis beam performance to be measured directly.

The far-field antenna pattern was obtained using the spherical near-field-to-far-field transform described in [14] and [19]–[21]. The 125-mm scan radius determined via the extrapolation measurement was used for the spherical near-field scan. The effective radius,  $r_0$  (as defined in ch. 19 of [14]), of the volume enclosing the feed horn was taken to be 20 mm. This fully encompassed the feed horn and angled waveguide feed transition. Using this and the expression  $\Delta\theta, \Delta\phi \leq 360/[2(kr_0 + 10) + 1]$  (given in [14, Ch. 19]), an upper limit on the angular sampling step sizes over the scan arc was determined to be  $\Delta\theta, \Delta\phi \leq 3.0^\circ$ . An actual step size of  $\Delta\theta = \Delta\phi = 1^\circ$  was used, which is within the sampling criteria. The measured far-field pattern normalized to the peak for the front hemisphere ( $0 \leq \theta \leq +90^\circ$ ,  $0 \leq \phi \leq 360^\circ$ ) for the total field  $|E_{\text{tot}}|$  is shown in Figure 8(a).

### FEED HORN SIMULATION

Numerical simulations were performed to determine the theoretical gain and pattern of the feed horn. The ideal horn geometry was used. The finite-element software package Ansys HFSS was used for this (mention of this product is not an endorsement but only serves to clarify what was done). The horn was modeled as being made from aluminum, and perfectly matched layer radiation boundary conditions were used. Mesh optimization was also performed within regions containing critical structures, such as inside the horn (including corrugations) and around the throat and aperture. The simulation was optimized until the change of  $|S_{11}|$  at the input port of the feed horn was reduced to  $\Delta|S_{11}| < 0.003$  between iterations. The gain was determined to be  $G_{\text{sim}} = 22.18$  dB from the simulation. The theoretical far-field pattern normalized to the peak for the front hemisphere ( $0 \leq \theta \leq +90^\circ$ ,  $0 \leq \phi \leq 360^\circ$ ) for the total field  $|E_{\text{tot}}|$  is shown in Figure 8(b).

### DISCUSSION

Comparing the simulated and measured gain and far-field patterns provides a measure of the antenna performance obtained using 3-D printing. A comparison reveals a reduction in the gain between the simulated and actual feed horn. The gain determined from the simulation was 22.18 dB, whereas the measured gain was 20.32 dB.

Figure 9 shows the decibel difference between the measured and simulated far-field patterns. The patterns themselves show good agreement within the first  $\pm 20^\circ$  centered on the main beam where the difference straddles the 0-dB level. The inflection in the difference appears at  $\theta = 17^\circ$  near where the peaks overlap as they should. Larger differences between the two patterns appear beyond about  $\pm 30^\circ$  from the main beam due to more local structure and increased energy in the sidelobes in the actual pattern versus the simulated pattern. This is indicative of roughness and imperfections in horn geometry imparting phase and amplitude errors across the aperture. A

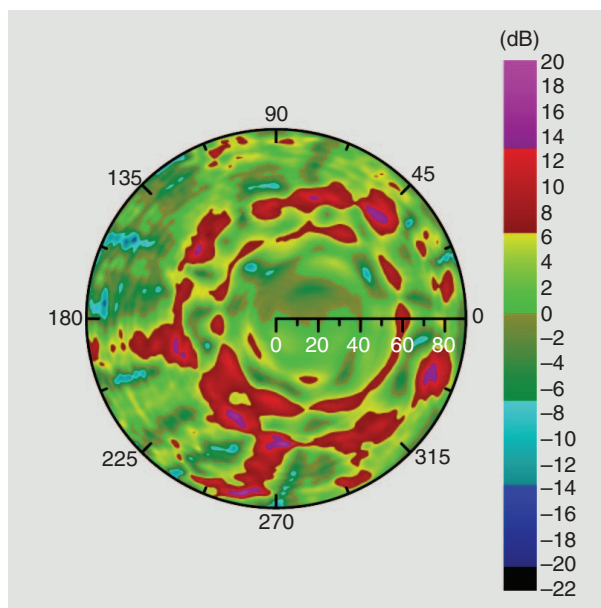


**FIGURE 9.** The decibel difference between the measured and the simulated normalized far-field patterns.

consequence of energy spreading into the sidelobes is the reduction in the gain from the simulated performance. As the simulated pattern has circular symmetry about the main beam (as it should for an  $HE_{11}$  mode), this local structure shows up as more drastic differences between the two patterns in excess of 10 dB in some places. Differences become dominated by simulation noise beyond about  $\theta = 70^\circ$ . However, averaging the difference within the  $35^\circ$  cone centered on the main beam (i.e., the angular subtense by the main reflector) shows an average agreement of  $\approx 1.1$  dB. Having good agreement (i.e., close to 0 dB) between the measured and simulated performance within the  $-3$  dB beamwidth from the main beam was most important for this application. These results show that this is indeed the case, and that 3-D printing the feed horn out of aluminum is a viable option for this CubeSat application.

### CONCLUSIONS

We presented a comparison of the measured and theoretical performance of a corrugated conical feed horn 3-D printed from the solid aluminum alloy AlSi10Mg using the PBF process. The feed horn was designed for the radiometer payload of the CubeSat PolarCube and operates at the atmospheric oxygen line of 118.7503 GHz. Spherical near-field and gain extrapolation measurements were performed at the CROMMA facility at NIST in Boulder, Colorado. The far-field antenna pattern over the front hemisphere of the feed horn was obtained using the spherical near-field to far-field transform.

In situ  $S_{11}$  extrapolation data were used to determine the optimum near-field scan radius to maximize dynamic range. This allowed sidelobe structure in the feed horn pattern to be detected up to 70 dB below the main beam peak while keeping mutual coupling between the probe antenna and feed horn to  $\Delta|S_{11}| \leq 0.1$  dB (peak to peak). Numerical simulations of the feed horn were used to determine theoretical performance (pattern and

gain). From these measurements, it was determined that the gain of the 3-D printed horn was  $20.32 \text{ dB} \pm 0.5 \text{ dB}$ , whereas the simulated gain was  $22.18 \text{ dB}$ . The far-field patterns showed good agreement within  $\pm 30^\circ$  of the main beam. The average difference within the  $35^\circ$  cone centered on the main beam (i.e., the angular subtense by the main reflector) shows agreement of  $\approx 1.1 \text{ dB}$ . Within the  $-3 \text{ dB}$  beamwidth from the main beam, agreement hovered around  $0 \text{ dB}$ , which was most important for this application. These results show that 3-D printing the feed horn out of aluminum is a viable option for this CubeSat application.

## ACKNOWLEDGMENTS

Special thanks goes to Glenda Alvarenga, Brian Sanders, and the PolarCube team at the University of Colorado Space Grant Consortium for providing the feed horn, support on the systems and designs for PolarCube, and many helpful discussions.

## AUTHOR INFORMATION

**Joshua A. Gordon** (josh.gordon@nist.gov) is a physicist in the Electromagnetics Division at the National Institute of Standards and Technology in Boulder, Colorado. His current research areas investigate new technologies for electric-field measurements. He is a Senior Member of the IEEE.

**David R. Novotny** (david.novotny@nist.gov) is an electrical engineer in the Electromagnetics Division at the National Institute of Standards and Technology in Boulder, Colorado. His current research areas are electromagnetic studies of antennas, propagation, and high-performance calibrations.

**Michael H. Francis** (michael.francis@nist.gov) is a physicist in the Electromagnetics Division at the National Institute of Standards and Technology in Boulder, Colorado. His current research areas are in the theory and practice of near-field measurements. He is a Senior Member of the IEEE.

**Ronald C. Wittmann** (ronald.wittmann@nist.gov) is a physicist in the Electromagnetics Division at the National Institute of Standards and Technology in Boulder, Colorado. His current research areas are in extending the applicability of near-field theory and measurement techniques. He is a Senior Member of the IEEE.

**Miranda L. Butler** (miranda.butler@nist.gov) is an undergraduate guest researcher at the National Institute of Standards and Technology in Boulder, Colorado. Her focus is on helping with the measurements and calibrations of radio frequency antennas.

**Alexandra E. Curtin** (alexandra.curtin@nist.gov) is a physicist in the Electromagnetics Division at the National Institute of Standards and Technology in Boulder, Colorado. Her current research focuses on antenna measurement optimization.

**Jeffery R. Guerrieri** (jeffrey.guerrieri@nist.gov) is an electrical engineer in the Electromagnetics Division at the National Institute of Standards and Technology in Boulder, Colorado. His research areas include antenna metrology and near-field measurements. He is a Member of the IEEE.

**Lavanya Periasamy** (Lavanya.Periasamy@colorado.edu) is currently pursuing her Ph.D. degree in electrical engineering at the University of Colorado, Boulder. She is a recipient of the NASA Earth and Space Science Fellowship in 2015 and 2016. She is a Student Member of the IEEE.

**Albin J. Gasiewski** (al.gasiewski@colorado.edu) is a professor of electrical and computer engineering at the University of Colorado (CU), Boulder, and director of the CU Center for Environmental Technology. He has developed and taught courses and guided research on electromagnetics, remote sensing, instrumentation, and wave propagation theory. He is a Fellow of the IEEE.

## REFERENCES

- [1] F. Khan. (2015, Aug.). Mobile Internet from the heavens. [Online]. Available: <https://arXiv:1508.02383>
- [2] L. Periasamy and A. J. Gasiewski, "Prelaunch antenna calibration of CubeSat MMW/SMMW radiometers with application to the PolarCube 3U temperature sounding mission," in *Proc. 2016 IEEE Int. Symp. Antennas and Propagation and U.S. National Committee for the Int. Union for Radio Science Nat. Radio Science Meeting*, pp. 5565–5568.
- [3] L. Periasamy and A. J. Gasiewski, "Precision design, analysis and manufacturing of quasi-optic lens/reflector antenna systems for CubeSat MMW/SMMW radiometers," in *Proc. 2015 U.S. National Committee for the Int. Union for Radio Science Meeting (Joint with AP-S Symp.)*, Vancouver, Canada, p. 265.
- [4] A. J. Gasiewski and J. T. Johnson, "Statistical temperature profile retrievals in clear-air using passive 118-GHz O<sub>2</sub> observations," *IEEE Trans. Geosci. Remote Sens.*, vol. 31, no. 1, pp. 106–115, Jan. 1993.
- [5] M. Klein and A. J. Gasiewski, "Nadir sensitivity of passive millimeter and submillimeter wave channels to clear air temperature and water vapor variations," *J. Geophys. Res.*, vol. 105, no. D13, pp. 17,481–17,511, July 2000.
- [6] P. Nayeri, M. Liang, R. A. Sabory-Garc, M. Tuo, F. Yang, M. Gehm, H. Xin, and A. Z. Elsherbeni, "3D printed dielectric reflect arrays: Low-cost high-gain antennas at sub-millimeter waves," *IEEE Trans. Antennas Propag.*, vol. 62, no. 4, pp. 2000–2008, 2014.
- [7] Z. Wu, J. Kinast, M. E. Gehm, and H. Xin, "Rapid and inexpensive fabrication of terahertz electromagnetic bandgap structures," *Opt. Express*, vol. 16, no. 21, pp. 16,442–16,451, 2008.
- [8] A. Macor, E. de Rijk, S. Alberti, T. Goodman, and J.-P. Ansermet, "Note: Three-dimensional stereolithography for millimeter wave and terahertz applications," *Rev. Sci. Instrum.*, vol. 83, no. 4, p. 46,103, 2012.
- [9] P. J. B. Claricoats and A. D. Oliver, *Corrugated Horns for Microwave Antennas*, (IEEE Electromagnetic Waves Series 18). Stevenage, U.K.: Peregrinus, 1984.
- [10] J. A. Gordon, D. R. Novotny, M. H. Francis, R. C. Wittmann, M. L. Butler, A. E. Curtin, and J. R. Guerrieri, "Millimeter-wave near-field measurements using coordinated robotics," *IEEE Trans. Antennas Propag.*, vol. 63, no. 12, pp. 5351–5362, 2015.
- [11] J. A. Gordon, D. R. Novotny, J. B. Coder, J. R. Guerrieri, and B. Stillwell, "Robotically controlled mm-wave near-field pattern range," in *Proc. Antenna Measurement Techniques Association Annu. Meeting Symp.*, 2012, vol. 34, pp. 384–389.
- [12] J. A. Gordon, D. Novotny, M. Francis, R. Wittmann, and J. Guerrieri, "The CROMMA Facility at NIST Boulder: A unified coordinated metrology space for millimeter-wave antenna characterization," in *Proc. Antenna Measurement Techniques Association Annu. Meeting Symp.*, 2014, vol. 36, pp. 351–356.
- [13] M. H. Francis, R. C. Wittmann, D. R. Novotny, and J. A. Gordon, "Spherical near-field measurement results at millimeter-wave frequencies using robotic positioning," in *Proc. Antenna Measurement Techniques Association Annu. Meeting Symp.*, 2014, vol. 36, pp. 231–234.
- [14] C. A. Balanis, *Modern Antenna Handbook*. Hoboken, NJ: Wiley, 2008.
- [15] D. R. Novotny, J. A. Gordon, M. Francis, R. Wittmann, A. E. Curtin, and J. R. Guerrieri, "Antenna measurement implementations and dynamic positional validation using a six axis robot," in *Proc. Antenna Measurement Techniques Association Annu. Meeting Symp.*, 2015, vol. 37, pp. 15–20.
- [16] J. A. Gordon, D. R. Novotny, and A. E. Curtin, "A single pixel touchless laser tracker probe," *J. CMSC*, vol. 10, no. 2, pp. 12–21, 2015.
- [17] A. C. Newell, R. C. Baird, and P. F. Wacker, "Accurate measurement of antenna gain and polarization at reduced distances by an extrapolation technique," *IEEE Trans. Antennas Propag.*, vol. 21, no. 4, pp. 418–421, 1973.
- [18] D. M. Kerns and E. S. Dayhoff, "Theory of diffraction in microwave interferometry," *J. Res. Natl. Bur. Stand.*, vol. 64B, no. 1, pp. 1–13, 1960.
- [19] P. F. Wacker, "Non-planar near-field measurements: Spherical scanning," National Bureau of Standards, Boulder, Co, NBSIR 75-809, June 1975.
- [20] J. E. Hansen, *Spherical Near-Field Antenna Measurements*. Stevenage, U.K.: Peregrinus, 1988.
- [21] R. C. Wittmann and C. F. Stubenrauch, "Spherical near-field scanning: Experimental and theoretical studies," National Institute of Standards and Technology, Boulder, CO, Internal Report NISTIR 3955, 1990.

